ORIGINAL RESEARCH ARTICLE

Influence of High-Velocity Oxy-fuel Sprayed Cr$_3$C$_2$-NiCr Coating on Corrosion and Wear Properties of AISI 2205

Rasim Göker Işık, Burçin Özbay Kısasöz, Gürkan Tarakçı, Sencer Süreyya Karabeyoğlu, Tolun Uğuz, and Alptekin Kısasöz

In this study, Cr$_3$C$_2$/10%NiCr layer was deposited on the AISI 2205 duplex stainless steel by the HVOF technique. Microstructural, tribological and corrosion behaviors of the coated and uncoated samples were investigated. The characterization studies were carried out by scanning electron microscopy, energy dispersive spectroscopy and optical microscopy. Moreover, dry sliding wear tests, corrosion tests and hardness measurements were performed to reveal the influence of Cr$_3$C$_2$-10%NiCr on the properties of AISI 2205 duplex stainless steel. Microstructural analysis revealed that proper bonding was achieved at the substrate-coating interface. On the other hand, it was observed that the coating structure consisted of chromium carbides and nickel-chromium binders. According to the corrosion test results, it was observed that the coating protected its structure and delayed the corrosion damage of the AISI 2205 alloy. The wear rate of the AISI 2205 alloy was reduced from $73.32 \pm 5.28 \times 10^{-5}$ mm^3·(Nmm)$^{-1}$ to $6.97 \pm 0.61 \times 10^{-5}$ mm^3·(Nmm)$^{-1}$ with Cr$_3$C$_2$-10%NiCr coating, as a result of the wear tests. In conclusion, test results showed that the Cr$_3$C$_2$-NiCr layer improved the corrosion and wear behavior of the AISI 2205 duplex stainless steel.

1. Introduction

Duplex stainless steel (DSS) is a type of stainless steel that consists of almost equal amounts of austenite and ferrite. Austenite offers general corrosion resistance and ductility, while ferrite provides mechanical strength and pitting resistance (Ref 1-6). DSSs are widely used in various industries such as desalination, shipbuilding, chemical storage, and petrochemical industries owing to their enhanced corrosion behavior and mechanical properties (Ref 7-10).

DSSs are generally used in chloride-enriched and acidic environments. Especially in the presence of chloride ions, the DSSs become sensitive to pitting corrosion (Ref 11-13). Accordingly, one of the most critical properties of DSSs is pitting corrosion resistance. Ferrite and austenite phase balance, elemental composition of phases, and presence of secondary phases are the main parameters for providing desired pitting corrosion resistance in DSSs (Ref 14-16). However, wear damages also occur in the DSSs, owing to the existence of solid particles in oil and gas production. Therefore, in addition to high corrosion resistance, DSSs are also required to have higher wear resistance in related applications (Ref 17).

Researchers have focused on improving the wear behavior of the DSSs by microstructural changes in studies related to the tribological properties of the DSSs. Correspondingly, these changes can be emphasized as varying the ferrite-austenite ratio by solution treatment, precipitation of the sigma phase and spinodal decomposition (Ref 18-20). As a result of microstructural transformations, the wear behavior of the DSSs can be improved, but these changes deteriorate the corrosion resistance of the structure (Ref 21-23). For this reason, the wear behavior of the DSSs should be improved by processes that do not cause any loss of corrosion resistance.

Surface treatment of DSSs is of interest because microstructural transformations are insufficient to improve wear resistance without impairing corrosion resistance. Surface treatments are used to provide higher tribological properties and corrosion behavior for the DSSs. Various surface engineering techniques have been applied to provide resistance to wear damage and corrosion environment. Subbiah et al. (Ref 24) emphasized that the erosion-corrosion behavior of the DSSs could be improved by the nitro-carburizing process. Calabokis et al. (Ref 25) studied the corrosion performance of the plasma nitrided DSSs, and it was stated that nitriding treatment produced significant corrosion performance improvement compared to untreated DSS. Neto et al. (Ref 26) showed that not only the corrosion resistance but also the wear behavior of duplex stainless steels was improved by the plasma nitriding process. Also, thermal spray technologies are used to fabricate coating to increase the wear and corrosion resistance of the steels (Ref 27-30). Manjunath Patel et al. (Ref 31) investigated the plasma spray

Rasim Göker Işık, Department of Metallurgical and Materials Engineering, Yildiz Technical University, 34210 Istanbul, Turkey; and Çimtaş Hassas İşleme Sanayi ve Ticaret Ltd. Şti., 16600 Bursa, Turkey; **Burçin Özbay Kısasöz** and **Gürkan Tarakçı**, Aluminum Test Training and Research Center (ALUTEAM), Fatih Sultan Mehmet Vakif University, 34445 Istanbul, Turkey; and **Sencer Süreyya Karabeyoğlu**, Department of Mechanical Engineering, Kirklareli University, 39000 Kirklareli, Turkey; **Tolun Uğuz**, Çimtaş Hassas İşleme Sanayi ve Ticaret Ltd. Şti., 16600 Bursa, Turkey; and **Alptekin Kısasöz**, Department of Metallurgical and Materials Engineering, Yildiz Technical University, 34210 Istanbul, Turkey. Contact e-mails: tolunuguz@yahoo.com and akisasoz@yildiz.edu.tr.

coating of Mo-Ni-Cr on DSS, and it was proved that wear loss was reduced in Mo-Ni-Cr coated DSS. On the other hand, Cr_3C_2-NiCr coatings applied using thermal spray processes were used to enhance the properties of the alloys (Ref 32-34). Significant corrosion resistance and wear behavior improvements have been achieved in various steel types coated with Cr_3C_2-NiCr by thermal spray processes (Ref 35-39). The properties of the Cr_3C_2-NiCr coated stainless steels have also been investigated. It was observed that the wear behavior and corrosion resistance of the AISI 316 and AISI 304 austenitic stainless steels were significantly improved by Cr_3C_2-NiCr coatings (Ref 40, 41). Manjunatha et al. (Ref 42) showed that Cr_3C_2-NiCr coatings increased the corrosion resistance of the AISI 316 stainless steel as well as oxidation resistance. Moreover, it was observed that NiCr metallic binder reduced the erosion rate of the structure. Otherwise, Hajare and Gogte (Ref 43) proved that the hot wear properties of the AISI 304 could be increased with the Cr_3C_2-based coatings. In addition, the use of high-velocity oxy-fuel spraying (HVOF), which is one of the thermal spray processes, reduces the thermal effect on the base material and provides high-quality coatings on stainless steel alloys (Ref 44-46).

However, studies on the coating of duplex stainless steels by thermal spray processes are very limited in the literature. Therefore, the present work has focused on the tribological behavior and corrosion resistance of the Cr_3C_2-10%NiCr coating on the AISI 2205 DSS. The HVOF process was used to fabricate the coating on the AISI 2205 DSS. The wear and corrosion behavior of the samples were characterized by dry sliding wear tests and electrochemical techniques, respectively.

2. Material and Methods

2.1 Materials

A cylindrical sample of AISI 2205 duplex stainless steel with dimensions of 20 mm in diameter and 20 mm in height was used as the substrate material. The AISI 2205 alloy was provided from Valbruna Turkiye. Also, Table 1 presents the chemical composition of the alloy.

Cr_3C_2-NiCr powder (Amperit 593) produced by Höganas AB; Sweden was used in the HVOF process. The content of the NiCr in powder was 10 wt.%. The chemical composition of the initial coating powder was given in Table 2.

In addition, the particle size distribution of the particles was investigated by the laser diffraction method with Mastersizer (Malvern Hydro 2000MU) and the average particle size of the coating powder was determined as 11.22 ± 4.50 μm. Also, the size distribution of particles is given in Fig. 1.

Before the coating process, XRD analyses were performed on AISI 2205 DSS and raw Cr_3C_2-10%NiCr powder to determine the phase properties. Moreover, XRD analysis was

performed on the HVOF-processed alloy to reveal the microstructure properties of the coating layer and substrate. The analysis was performed between 30° and 90° 2θ range by Rigaku Miniflex 600 at a scanning rate of 1° min^{-1}. The PDXL program was used to classify detected patterns via Joint Committee on Powder Diffraction Standards (JCPDS) database. On the other hand, a phase balance of the AISI 2205 DSS was determined by Rietveld analysis of XRD results.

2.2 HVOF Thermal Spraying Process

The coatings were deposited on specimens with a DJ2600 HVOF spray gun (Oerlikon Metco, Switzerland). During the spraying process, hydrogen, oxygen, nitrogen, and air were used as a fuel, an oxidizing gas, a carrier gas and a shroud, respectively. Specimens were fixed to a turntable, and one face of the specimens was coated by using summarized parameters given in Table 3. Before the coating process, one pass of preheating was applied to the specimens with HVOF flame without powder-feed up to 65 °C. All movements of the spray gun and turntable were controlled and monitored by a six-axis robot (IRB 2600, ABB, Switzerland).

2.3 Microstructure Characterization of Coating

The microstructural properties of a coating were determined by scanning electron microscopy (SEM-Hitachi SU3500) examinations. The SEM analyses were performed from the cross section and top surface of the Cr_3C_2-NiCr layer. Energy dispersive spectroscopy (EDS, Oxford instrument) mapping analyses were carried out to determine elemental distribution in the coating. Moreover, the porosity content of the coating was investigated by image analyses on SEM micrographs.

2.4 Hardness

Hardness values of the coating and substrate were investigated by Vickers hardness tests (Shimadzu G21D) by a 30 g test load. The hardness of the AISI 2205 DSS was determined before and after the HVOF process. The hardness distribution of the coating was investigated and compatible with Singh and Kaur (Ref 47). The hardness distribution was determined by measurements at 30 μm intervals from the surface to the substrate at the cross section. An average of at least 10 indents was given as a hardness value.

Table 2 Chemical composition of the initial powder (wt.%)

C	Fe	Ni	Cr
12.11	1.87	5.17	Bal.

Table 1 Chemical composition of the AISI 2205 DSS alloy (wt.%)

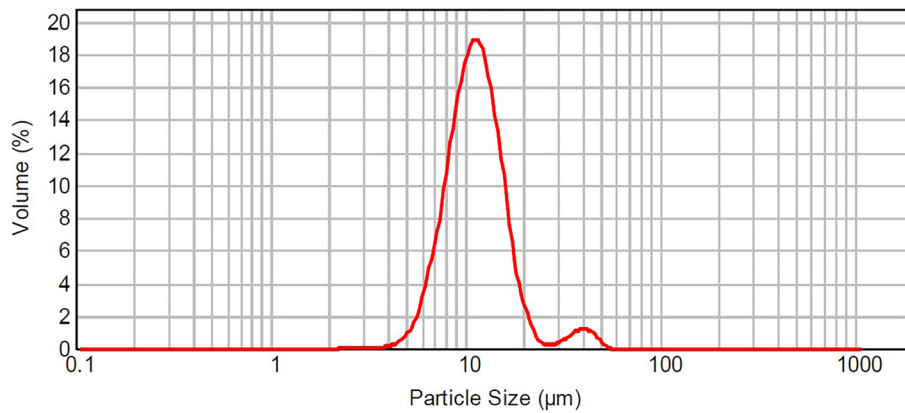| Cr	Ni	Mo	Mn	Si	C
22.700	5.090	3.190	1.460	0.500	0.019
Cu	**W**	**P**	**S**	**N**	**Fe**
0.500	0.047	0.030	0.001	0.156	Bal.

Fig. 1 Size distribution of the Cr_3C_2-10%NiCr powder

Table 3 The process parameters used in HVOF spray deposition

Fuel gas (H_2)flow rate, l min^{-1}	Oxygenflow rate, l min^{-1}	Shroud (air)flow rate, l min^{-1}	Carrier gas (N_2)flow rate, l min^{-1}	Feed rate, g min^{-1}	Stand-off distance(SoD),mm
550	100	300	18	35	250

2.5 Corrosion

Electrochemical corrosion behavior was investigated with a triple electrode system by Ivium Compactstat. The electrode system included a test sample, Ag/AgCl solution and platinum. Working and counter electrode surface area ratio was settled to 1:4. Moreover, the reference electrode potential value was identified as 0.065 mV. Electrochemical impedance spectroscopy (EIS) and potentiodynamic polarization (PDP) tests were carried out to reveal the electrochemical corrosion behavior of the samples.

The 3.5 wt.% NaCl solution was used in PDP tests to simulate the seawater environment. The chloride concentration of the corrosion environment significantly affects the corrosion behavior of stainless steel (Ref 48). Accordingly, PDP tests were carried out in 3.5 wt.% NaCl concentration to determine the influence of Cr_3C_2-10%NiCr coating on the polarization behavior of the AISI 2205 DSS. The test samples were prepared according to ASTM G5-94. Before PDP experiments, the samples were held in the 3.5 wt.% NaCl solution for 30 minutes, followed by open circuit potential (OCP) tests performed for 30 minutes. Subsequently, the PDP tests were performed with 0.5 mV s^{-1} scan rate ranging from − 0.25 to 1.5 V against the OCP. Moreover, corrosion current density (i_{corr}), corrosion potential (E_{corr}), and corrosion rate were calculated from the PDP test results.

The EIS tests were performed in a 3.5 wt.% NaCl solution. Before EIS experiments, a similar procedure was applied to samples as PP tests. The EIS tests were applied at the OCP over a frequency range of 0.1-10 kHz with an AC current of 10 mA. Nyquist and Bode plots were acquired by IviumSoft software.

In addition, immersion corrosion tests were applied to the HVOF Cr_3C_2-10%NiCr coated and uncoated samples to fully reveal the influence of the HVOF spray coating on the corrosion behavior of the AISI 2205 DSS. The immersion tests were carried out as described in ASTM G48 Method A. The coated and uncoated AISI 2205 alloys were kept in a
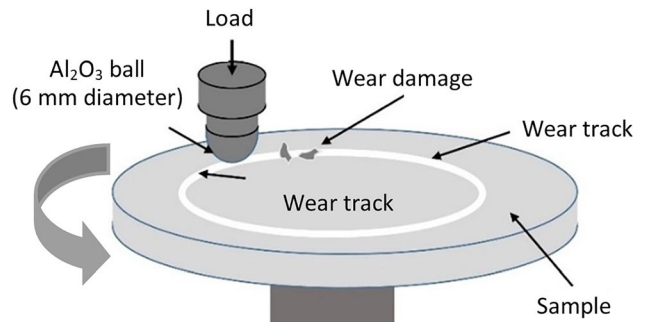

Fig. 2 The schematic illustration of the dry sliding wear test set up

standard solution ($FeCl_3$-6 wt.%) for 72 hours. After the immersion tests, corrosion products were removed by dipping into acetone following rinsing with distilled water. The alloys were also weighed before and after the immersion test to determine the corrosion loss. After the PP and immersion corrosion tests, optical microscopy and SEM examinations were carried out to determine the corrosion damage.

2.6 Wear

The wear behavior of the samples was studied at room temperature in dry sliding conditions by a ball-on-disk tribometer using the 6 mm diameter Al_2O_3 counterface. The wear test setup is given in Fig. 2. The tests were repeated 3 times for each sample. Before wear tests, samples were polished, and the arithmetic roughness was settled as approximately 1 μm for each surface. Moreover, the parameters were determined as 200 m sliding distance, 0.1 m s^{-1} sliding velocity, and 5 N and 20 N test loads.

Volume loss (V) was calculated via Eq 1, according to ASTM G99-17;

$$V = 2\pi R \left[r^2 \sin^{-1}(d/2r) - (d/4)(4r^2 - d^2)^{1/2} \right] \quad (Eq\ 1)$$

The "d" is the wear track width, "r" is the ball radius, and "R" is the wear track radius. The image analyses were performed to identify the "R" and "d" values. Also, the wear rate values were determined by using Eq 2;

$$WR = V/LP \qquad (Eq\ 2)$$

In Eq 2, "P" is the applied load, and "L" is the sliding distance. In addition, the coefficient of friction (CoF) was measured by the tribometer.

Moreover, the worn surface of the coated and uncoated alloys was analyzed by SEM. Also, wear scars of the coated and uncoated AISI 2205 alloys were examined by the Sofar 3D profilometer, and the depth and width values of the wear scars were determined.

3. Results and Discussion

3.1 XRD Analyses

The XRD analyses can be seen in Fig. 3. The typical peaks of the body-centered cubic ferrite (reference no: 01-085-1410) and face-centered cubic austenite (reference no: 98-005-1420) phases were obtained for the AISI 2205 DSS alloy. Moreover, the presence of any secondary phase was not observed. The coating powder included the characteristic peaks of the Cr_3C_2
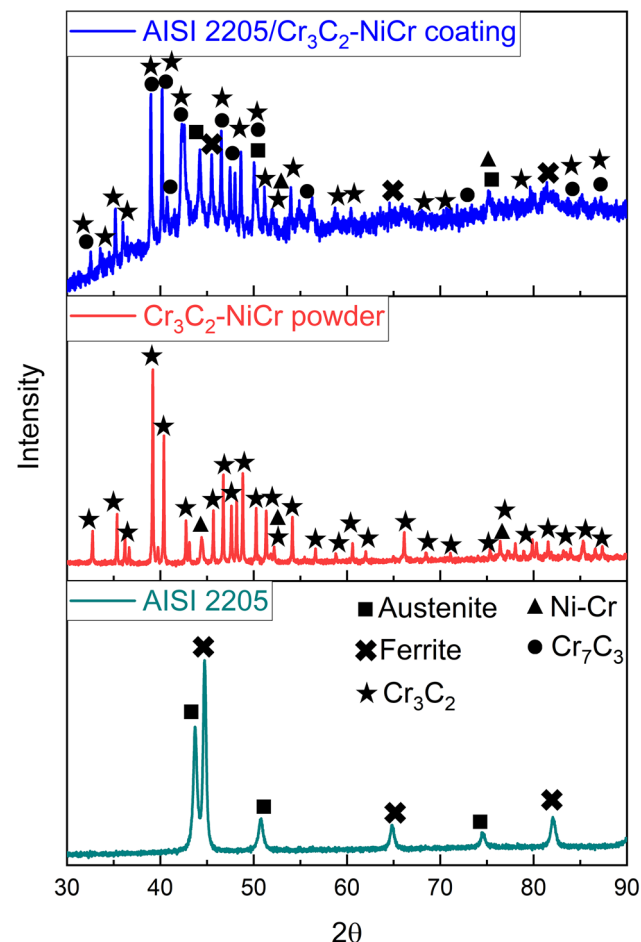

Fig. 3 XRD analyses of the substrate, powder and HVOF-processed alloy

(reference no: 01-071-2287) and nickel-chromium solid solution (reference no: 01-087-0712). In the powder structure, only two expected phases were detected. However, the HVOF-processed alloy consisted of the Cr_3C_2 (reference no: 01-071-2287), Cr_7C_3 (reference no: 98-005-0450) and nickel-chromium (reference no: 01-087-0712) with the typical peaks of the ferrite (reference no: 01-085-1410) and austenite (reference no: 98-005-1420) phases. Thermal inputs during the application of the HVOF provided the formation of desired transformation conditions in the deposited layer. Thus, the process caused the formation of Cr_7C_3 carbides in the coated layer together with the Cr_3C_2 main carbide structure (Ref 49).

3.2 Microstructure Analysis of the Substrate and Powder

In order to determine the initial phase structure of the AISI 2205 substrate, the Rietveld analysis was performed by using XRD results (Ref 50). According to analysis, AISI 2205 DSS consisted of 49.8% body-centered α (ferrite) and 50.2% face-centered γ (austenite) phases.

The microstructure of the substrate taken by optical microscopy is given in Fig. 4(a). The microstructure of the AISI 2205 was compatible with the XRD analysis. The α (ferrite) and γ (austenite) phases were seen as dark and light, respectively. Moreover, as mentioned earlier in the XRD results, no sigma phase precipitation was observed.

As a result of XRD analyses and microstructure examinations, it was observed that the AISI 2205 DSS alloy consists of the desired ferrite-austenite phase ratio and does not contain any secondary phases. It was determined that the alloy had suitable properties for the coating process with these microstructural features.

The SEM analysis was performed on the raw Cr_3C_2-NiCr powder to investigate the morphology of the particles. The SEM micrograph of the raw Cr_3C_2-NiCr powder is given in Fig. 4(b). It was determined that the initial powder has an angular structure. In addition, the particle size was determined in x and y coordinates by ImageJ software. The particle size measurements were carried out from 10 different areas, and the average particle size was determined as $12.42 \pm 5.81\ \mu m$. The average particle size value obtained from the SEM micrograph was compatible with the average particle size value obtained by Mastersizer analysis.

3.3 Microstructure and Hardness of the Coating

The SEM surface images of the Cr_2C_3-NiCr are given in Fig. 4(c). According to the surface image, it was seen that the coating was successfully formed. In addition, splats (indicated by white arrows), which typically occur in thermal spray processes, were observed in the surface image (Ref 51). On the other hand, two different regions as bright and dark were observed on the coated surface. Dark and bright regions represented the carbide-rich phase and NiCr metallic phase, respectively (Ref 41).

The mapping analysis performed on the cross section of the Cr_3C_2-NiCr coated AISI 2205 DSS was given in Fig. 5. The coating material consisted of chromium carbides and nickel-chromium metallic binder (Ref 52). Accordingly, a structure with homogenous chromium distribution was observed due to the chromium-based coating material. In the regions, where nickel-chromium metallic binder structure was present in the coating, a nickel-rich elemental distribution was obtained. In addition, oxidation of the chromium occurred in the coating
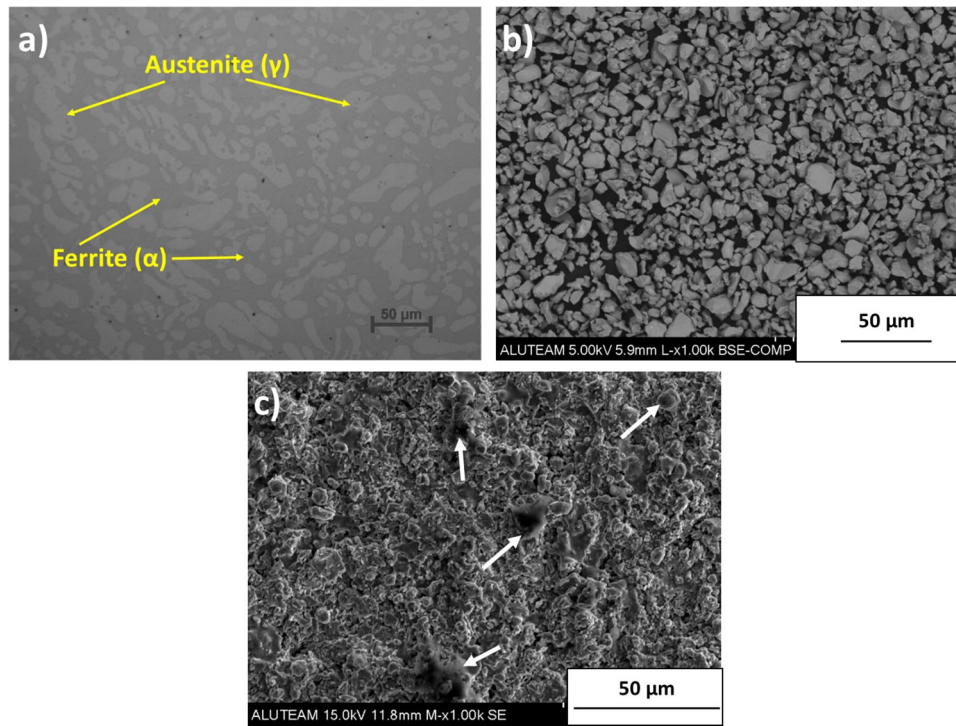
Fig. 4 Micrographs of (a) Initial AISI 2205 DSS (optical microscopy), (b) Raw Cr_3C_2-NiCr powder (SEM-Back-scatter electrons), (c) Surface image of the Cr_3C_2-NiCr coating (SEM-Secondary electrons)

structure due to the HVOF process (Ref 53). Therefore, a homogeneous and dense oxygen distribution was also determined in the mapping analysis.

The microstructure of the Cr_3C_2-NiCr coated AISI 2205 DSS can be seen in Fig. 6. The coating structure was deposited on the AISI 2205 DSS substrate with the help of an HVOF gun and a multi-pass process (Fig. 6a). The multi-pass HVOF process led the formation of uniform coating structure, as seen in Fig. 5 and 6(a). Moreover, the characteristic layered, and spat-like structure was obtained due to the deposition and re-solidification of molten or semi-molten droplets (Ref 52).

Cracks are formed in the thick coatings due to thermal effects and internal stress. The corrosion environment can easily pass the coating layer owing to existence of cracks and the corrosion resistance of the structure reduces. Contrary, thin coatings cannot protect the substrate in aggressive environments (Ref 38). In addition, heterogeneous coating structure and existence of the defects like porosity reduce the protectiveness of the coating layer (Ref 54). Thus, it is critical to obtain a homogenous coating layer in appropriate thickness for providing desired properties. The average coating thickness was determined as 245 ± 5 μm in our study. It was reported that the standardized cermet coating thickness was approximately 300 μm and increasing coating thickness leads to the depletion of the coating and formation of large cracks (Ref 38, 55). Accordingly, it was determined that the appropriate coating thickness was obtained to provide the desired structure and properties. At an average distance of 45.1 ± 5 μm from the surface of the coating, a denser pore formation was observed compared to the overall structure of the coating (Fig. 6d-zone 3). In the HVOF process, the molten material shrinks upon cooling and the shrinkage is compensated by newly melted particles (Ref 37). However, the porosity content was increased in the top layer due to the lack of feeding effect.

The cross section of the coating consisted of carbides (A), nickel-chromium metallic structure (B), Cr_2O_3 oxide (C), pores (D) and cracks (E), as seen in Fig. 6(b), (c) and (d). The Cr_2O_3 was observed in low amounts, and the formation of these oxides was related to the oxidation of in-flight particles between the passes (Ref 51). The coating process was applied by multi-pass deposition. The heat input during the deposition of a layer caused a thermal effect on the previous layers. Because of the thermal inputs, a slower cooling rate was obtained in the initial deposited layers (Fig. 6b-zone 1, c-zone 2) and the angular raw powder transformed to the spherical structure. Contrary, in the upper layer of the coating, a higher cooling rate was obtained due to the absence of inter-pass thermal effects. Therefore, a higher cooling rate was obtained in the deposited layer and increasing cooling rate values caused the formation of defects like cracks and porosity in a higher manner (Ref 55). Moreover, porosity formation was observed in the upper layer of the coating as seen in Fig. 6d-zone 3. It was considered that porosity was formed by the removal of carbides during the microstructural preparation owing to weaker particle bonding in the upper layer. On the other hand, the Cr_3C_2 carbides were partially decomposed to Cr_7C_3 carbides during the HVOF process (Ref 51). The carbide size was increased, and the carbide shape was transformed from spherical to angular with the transition from the bottom layer to the top layer (Fig. 6-zone 1 to zone 3). The starting powder contained large and angular-shaped carbides. The multi-pass deposition process led to transformation of the carbide structure in the previous layer and the carbides became spherical and smaller in size. However, the carbide structure of the starting powder was preserved in the top layer due to the lack of a re-melting effect.

The hardness distribution of the Cr_3C_2-NiCr layer was given in Fig. 7. The hardness of the AISI 2205 alloy was determined
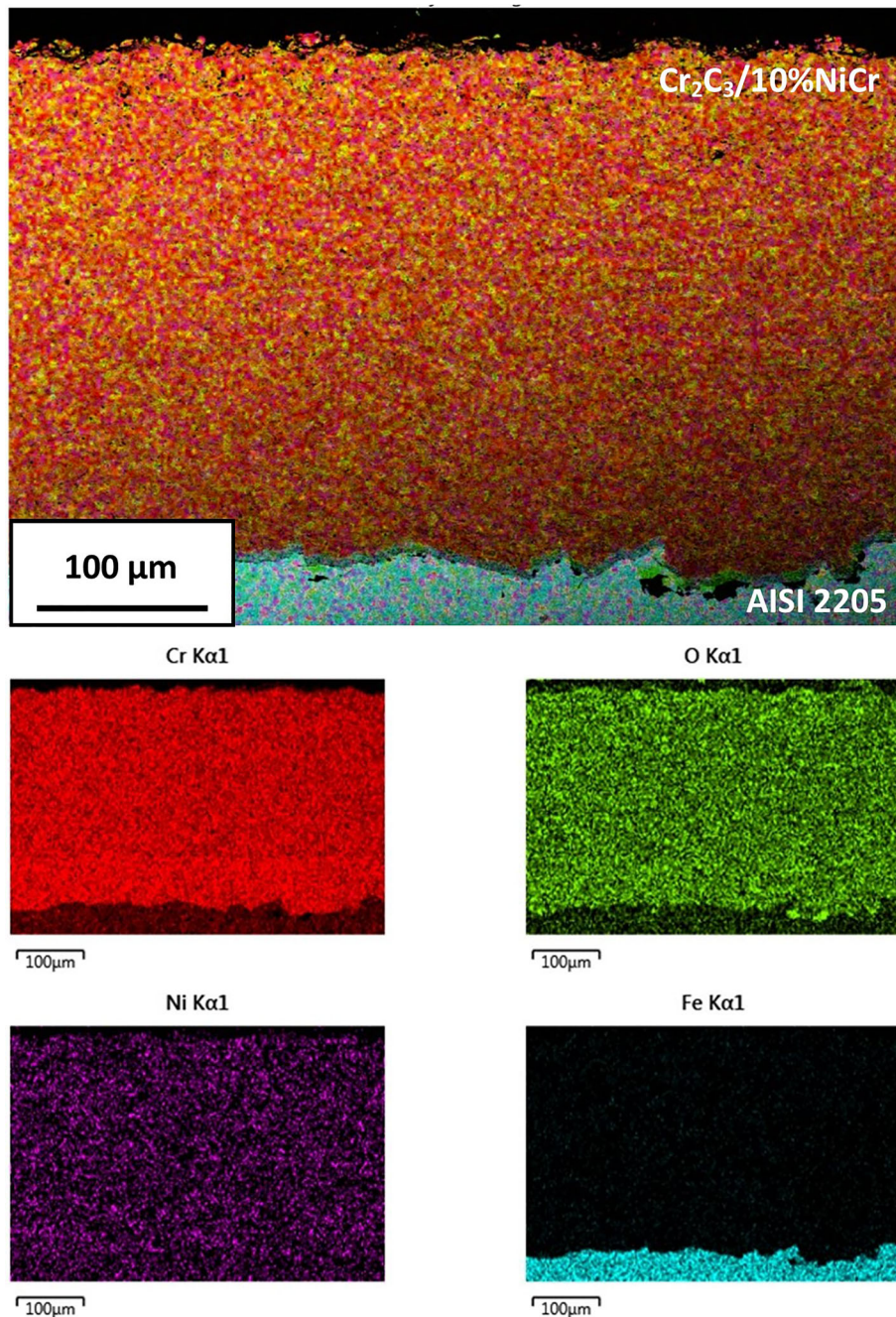
Fig. 5 EDS mapping of the Cr_3C_2-NiCr coated AISI 2205 DSS

as 275 ± 5 HV after the HVOF process. The hardness of the as-received AISI 2205 alloy was measured as 271 ± 4 HV, and it was observed that there was no obvious change in the hardness of the substrate before and after the HVOF process. It can be deduced from the hardness investigations that the HVOF process did not influence the microstructure of the substrate. Moreover, the hardness of the coating was measured at 655 HV and 683 HV values at the top layers. The hardness increased toward the bottom layers, and the value increased up to 972 HV. Also, the presence of coarser angular carbides caused a decrease in hardness values. Contrarily, the spherical and fine-grained carbide structures improved the hardness values at the bottom layers.

3.4 Corrosion

The obtained OCP values prior to PDP tests can be seen in Fig. 8(a). In the Cr_3C_2-NiCr coated AISI 2205 DSS sample, the initial potential was determined as 0.016 V, and the measurement ended with a value of 0.055 V. During the OCP measurement, the potential value increased slightly at the beginning and then reached a stable condition. When the open circuit potential measurement of AISI 2205 DSS alloy was examined, it was observed that the initial value was -0.237 V. The potential value increased during the test, and the measurement ended at -0.112 V. An increasing potential value during OCP measurement indicated that a protective film was formed
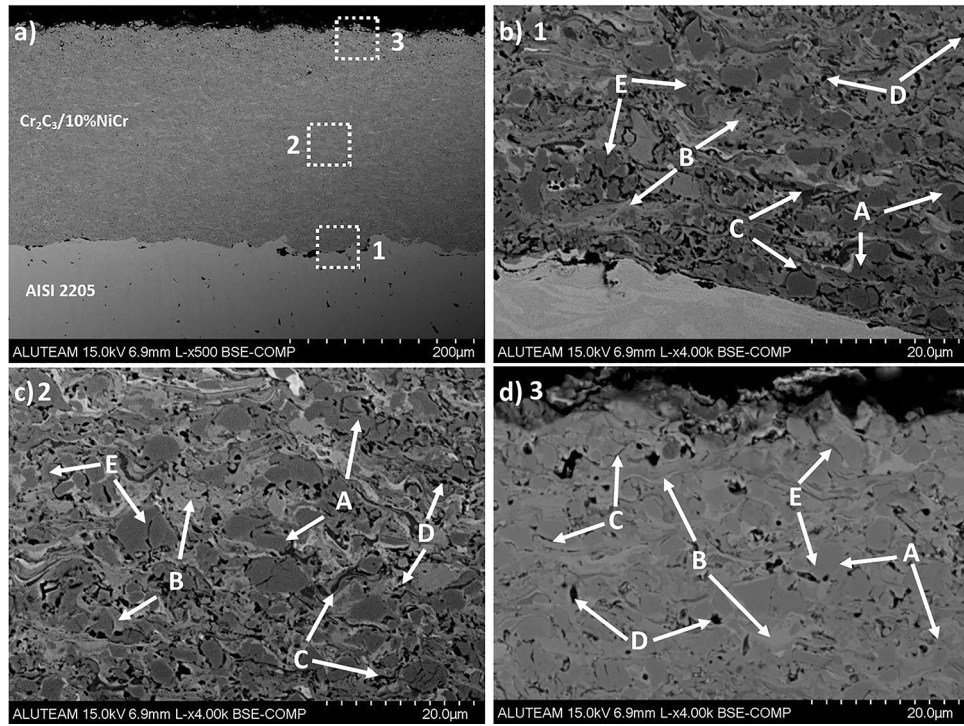
Fig. 6 SEM cross section image of the Cr$_3$C$_2$-NiCr coated AISI 2205 DSS. (a) Cross section of the coating. (b) Initial layer of the coating. (c) Middle layer of the coating. (d) Upper layer of the coating
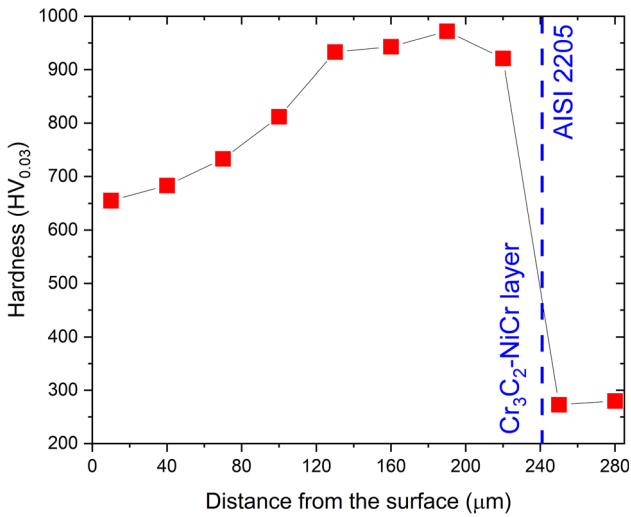

Fig. 7 Hardness distribution of a coated layer

potential (E_{corr}) determined as $-$ 0.1482 V for AISI 2205 alloy was shifted to a more noble value and measured as $-$ 0.0738 V by applying the Cr$_3$C$_2$-NiCr coating to the alloy. On the other hand, the corrosion current density increased from 6.64×10^{-8} A cm^{-2} to 59.55×10^{-8} A cm^{-2} with the existence of the coating. This change in corrosion current density was also reflected in the corrosion rate values, and the values of the coated sample increased from 0.0007113 to 0.006376 mm·year^{-1}. As it is well known, E_{corr} indicates the potential for corrosion initiation, while i_{corr} indicates the rate of dissolution during the corrosion of the structure (Ref 58). The Cr$_3$C$_2$-NiCr coating increased the E_{corr} value and caused corrosion to initiate at higher potential values, but once corrosion started, it caused much faster dissolution kinetics compared to uncoated AISI 2205 DSS alloy. The Cr$_3$C$_2$-NiCr layer provided a retarding effect on the formation of corrosion in 3.5 wt.% NaCl environment. However, the structure of the deposited layer consisting mainly of Cr$_3$C$_2$ and Cr$_7$C$_3$ carbides caused the increase in dissolution kinetics with the arising of corrosion, resulting in an increased corrosion rate compared to the uncoated sample.

Figure 9 shows the SEM micrographs of the corrosion surface taken after PDP tests. Corrosion damages on the surface of coated and uncoated samples were shown with white circles and white arrows, respectively. It was seen that the corrosion damage on the surface of the coated sample occurred on the whole surface with the homogenous dissolution of the Cr$_3$C$_2$-NiCr layer (Fig. 9a). However, in the uncoated AISI 2205 alloy, it was observed that corrosion damage occurred with the formation of localized pits (Fig. 9b). DSSs have a protective chromium oxide layer on the surface, and it improves corrosion resistance in the aggressive environments (Ref 59). However, corrosion damage occurs locally on the DSS surface by pit formations in chloride-containing environments (Ref 60).

on the surface, and the corrosion resistance of the sample increased over time (Ref 56). An increasing trend of the OCP for AISI 2205 DSS alloy could be attributed to the formation of a protective oxide-based layer (Ref 57).

The Tafel curves and the test results can be seen in Fig. 8(b) and Table 4, respectively. AISI 2205 DSS sample and Cr$_3$C$_2$-NiCr coated AISI 2205 DSS showed a similar polarization characteristic. Also, the corrosion rate, corrosion current density (i_{corr}), and corrosion potential (E_{corr}), values were determined by exploration of the polarization curves. The

Compatibly, pits were observed on the corroded surface of the uncoated sample. On the other hand, coated AISI 2205 DSS alloy tended to dissolve along the whole surface. Although the Cr$_3$C$_2$-NiCr layer slightly increased the corrosion rate of AISI 2205, the corrosion mechanism changed from heterogeneous dissolution in the form of pitting to homogeneous dissolution. Thus, dissolution occurred over the entire surface.

In order to reveal the influence of Cr$_3$C$_2$-NiCr coating on the corrosion behavior of AISI 2205 DSS clearly, immersion corrosion tests in FeCl$_3$ solution were applied to coated and uncoated samples. Also, the microstructure analyses were performed after the immersion corrosion tests, and the micro-

graphs were given in Fig. 10. Before and after the tests, the coated and uncoated alloys were weighed, and the weight loss values were determined. As a result of the immersion corrosion test, the weight loss values of AISI 2205 DSS and Cr$_3$C$_2$-NiCr coated AISI 2205 DSS samples were determined as 10.89 mg cm^{-2} and 43.69 mg cm^{-2}, respectively. The weight loss values were compatible with the corrosion rate values obtained with the PDP tests. In addition, pits occurred on the corrosion surface of the uncoated sample (Fig. 10b), whereas a homogeneous dissolution was observed in the coated sample (Fig. 10a). Although higher dissolution tendency and corrosion rate were determined in the coated sample, it was observed that the coating layer maintained its structure on the substrate after the immersion test. Accordingly, it was observed that although the coating layer had a higher corrosion rate compared to AISI 2205 DSS, it protected the substrate during the immersion test.
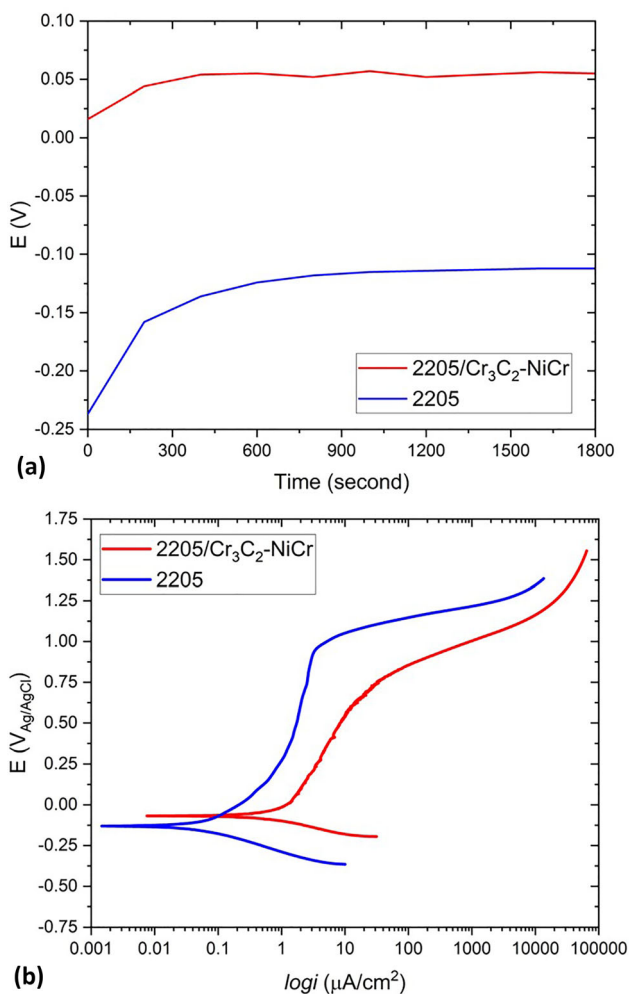

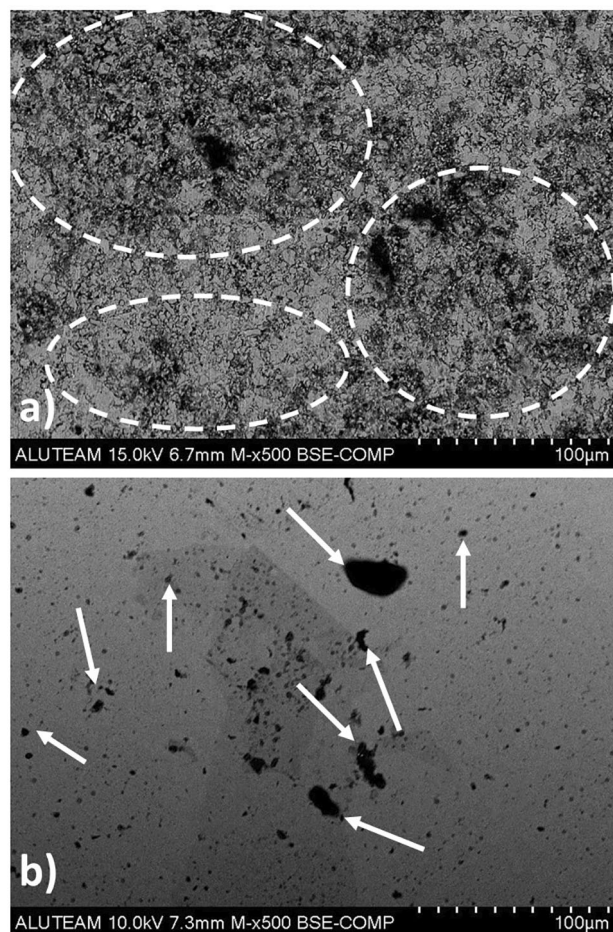**Fig. 8** Potentiodynamic polarization test results. (a) OCP curves, (b) Tafel curves

Fig. 9 SEM images of the corrosion surface after potentiodynamic polarization tests. (a) Cr$_3$C$_2$-NiCr/AISI 2205 DSS, (b) AISI 2205 DSS.

Table 4 Potentiodynamic polarization test results

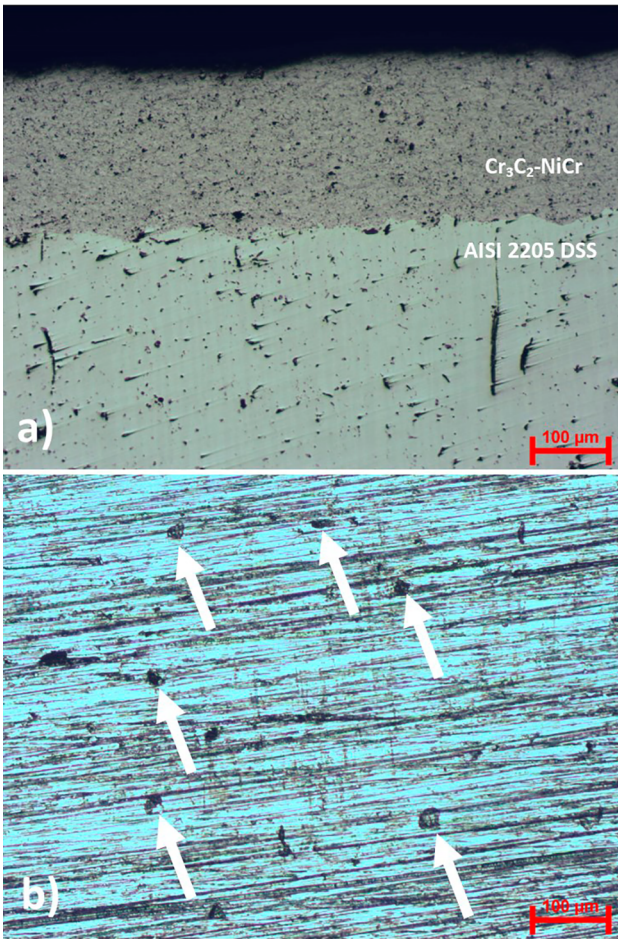| Sample	E_{corr},V	i_{corr},A cm^{-2}	Corrosion rate, mm year^{-1}
AISI 2205	− 0.1482	6.64 × 10^{-8}	0.0007113
AISI 2205/Cr$_3$C$_2$-NiCr	− 0.0738	59.55 × 10^{-8}	0.0063760

Fig. 10 The microstructure of the samples after immersion corrosion tests. (a) Cross section of the Cr_3C_2-NiCr/AISI 2205 DSS, (b) Surface of the AISI 2205 DSS

For AISI 2205 DSS alloy, where corrosion damage occurs by pit formation, the corrosion reactions can be expressed as follows (Ref 61):

The 2205 DSS dissolved to produce Fe^{2+} and Cr^{3+} ions during the pitting corrosion (Eq 3 and 4).

$$Fe \rightarrow Fe^{2+} + 2e^- \tag{Eq 3}$$

$$Cr \rightarrow Cr^{3+} + 3e^- \tag{Eq 4}$$

Hydrolysis reactions occurred with the presence of Fe^{2+} and Cr^{3+} ions (Eq 5 and 6).

$$Fe^{2+} + H_2O \rightarrow FeOH^+ + H^+ \tag{Eq 5}$$

$$Cr^{3+} + H_2O \rightarrow CrOH^{2+} + H^+ \tag{Eq 6}$$
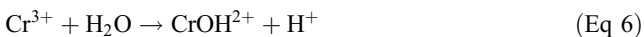
The dissolution of the bulk metal became dominant with the occurrence of the metastable pitting. Therefore, the possibility of the formation of a chloride-containing salt film was included in the model (Eq 7 and 8).

$$Fe^{2+} + Cl^- \rightarrow FeCl^+ \tag{Eq 7}$$

$$Fe^{2+} + 2Cl^- \rightarrow FeCl_2 \tag{Eq 8}$$

On the other hand, corrosion damage of the Cr_3C_2-NiCr coated AISI 2205 DSS occurred by the homogenous dissolution of the corrosion surface. Accordingly, the corrosion occurred by separate dissolution reactions of chromium and nickel. The reactions can be expressed as Eq 9 and 10 (Ref 62).

$$Ni + H_2O \rightarrow NiO + 2H^+ + 2e^- \tag{Eq 9}$$

$$Cr^{3+} + H_2O \rightarrow CrOH^{2+} + H^+ \tag{Eq 10}$$
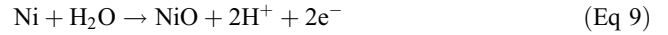
Thus, despite the high corrosion rate of the coating, the AISI 2205 was protected, and corrosion damage did not occur on the substrate. Considering the presence of corrosion damage with pit formation in the uncoated sample, the Cr_3C_2-NiCr coating had a positive effect on the corrosion behavior of AISI 2205 DSS alloy in chloride ions environment.

Figure 11(a) and (b) depicts the Nyquist and Bode plots after the EIS tests performed in 3.5 wt.% NaCl solution. The Nyquist plots had a randel-like feature (Fig. 11a). The coated sample showed a nearly linear characteristic that could be attributed to the double-layered surface. Despite that, the impedance value of the AISI 2205 DSS alloy was decreased. The decrease in the impedance value could be related to pitting corrosion, as determined by potentiodynamic polarization and immersion corrosion tests. The phase angle Bode plots of the samples were given in Fig. 11(b). The peak angle for AISI 2205 DSS alloy shifted to lower frequency values compared to Cr_3C_2-NiCr coated AISI 2205 alloy. As mentioned earlier, coated sample corroded by the homogenous dissolution of the surface, and this led to the formation of more corrosion products. Therefore, the peak angle was reached at higher frequency values in the coated sample (Ref 40).

The equivalent electrical circuits used to fit the impedance data for AISI 2205 and AISI 2205/Cr_3C_2-NiCr were given in Fig. 11(c) and (d), respectively. Also, $R_{solution}$, $R_{substrate}$, $R_{coating}$, $CPE_{substrate}$ and $CPE_{coating}$ represented the solution resistance, substrate resistance, coating resistance, capacitance of the substrate and capacitance of the coating, respectively. The EIS results obtained from the fitted curves were summarized in Table 5. The measured capacitance was often not ideal, and Q is determined as the constant phase element (Ref 63). The $R_{solution}$ was obtained at similar values since the tests were carried out in the 3.5% NaCl solution. The $R_{coating}$ was found as 2.899×10^3, and it was very high compared to $R_{solution}$, indicating the corrosion resistance of the Cr_3C_2-NiCr layer in the 3.5% NaCl solution. The $Q_{coating}$ was determined lower than the $Q_{substrate}$. It can be related to higher thickness of the Cr_3C_2-NiCr layer, compared to protective chromium oxide layer on the AISI 2205 alloy. On the other hand, $Q_{substrate}$ value of the coated AISI2205 was lower than $Q_{substrate}$ value of the uncoated AISI 2205. It indicated that the solution/substrate interaction was decreased with the presence of the Cr_3C_2-NiCr layer. In addition, increases in $R_{substrate}$ value was compatible with these findings, indicating the increases in corrosion resistance of the AISI 2205 surface. It can be stated from EIS test results that Cr_3C_2-NiCr
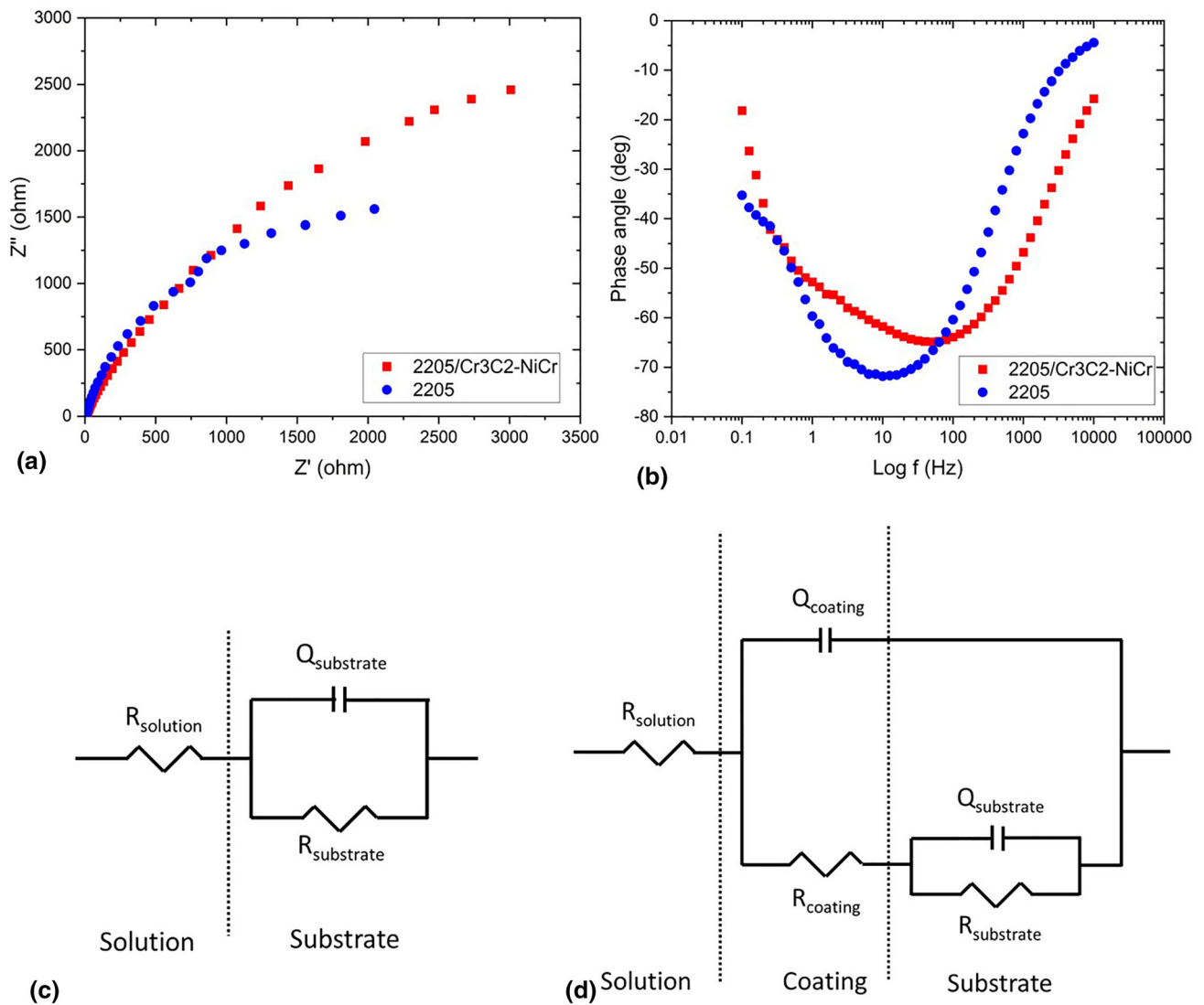
Fig. 11 EIS results of the samples. (a) Nyquist plots, (b) Bode plots and Equivalent circuits fit the impedance data for (c) AISI 2205, (d) AISI 2205/Cr_3C_2-NiCr

Table 5 EIS results of the samples

Sample	$R_{solution}$, Ω cm^2	$R_{coating}$, Ω cm^2	$R_{substrate}$, Ω cm^2	CPE$_{coating}$, Y_0, (Ω^{-1} cm^{-2} s^a)^n	CPE$_{substrate}$, Y_0, (Ω^{-1} cm^{-2} s^a)^n
AISI 2205	6.544	…	2.451×10^3	…	6.992×10^{-4}
AISI 2205/Cr_3C_2-NiCr	6.619	2.899×10^3	3.783×10^3	1.017×10^{-4}	1.509×10^{-4}

coating has positive effect on the corrosion behavior of the AISI 2205 DSS.

3.5 Wear

Figure 12 shows the micrographs of the worn surface of samples. The worn surface of the AISI 2205 including the grooves and debris represents the abrasive wear mechanism.

Especially, the surface of the sample worn at 5N consisted of a fine wear debris and the series of parallel grooves (Fig. 12a), which shows that aggressive abrasive wear is dominant. Moreover, the formation of ridges and coarse debris with increasing test load shifted the wear mechanism toward less abrasion (Fig. 12c).

On the other hand, the worn surface of the Cr_3C_2-NiCr coated AISI 2205 DSS worn at 5 N consisted of cracks
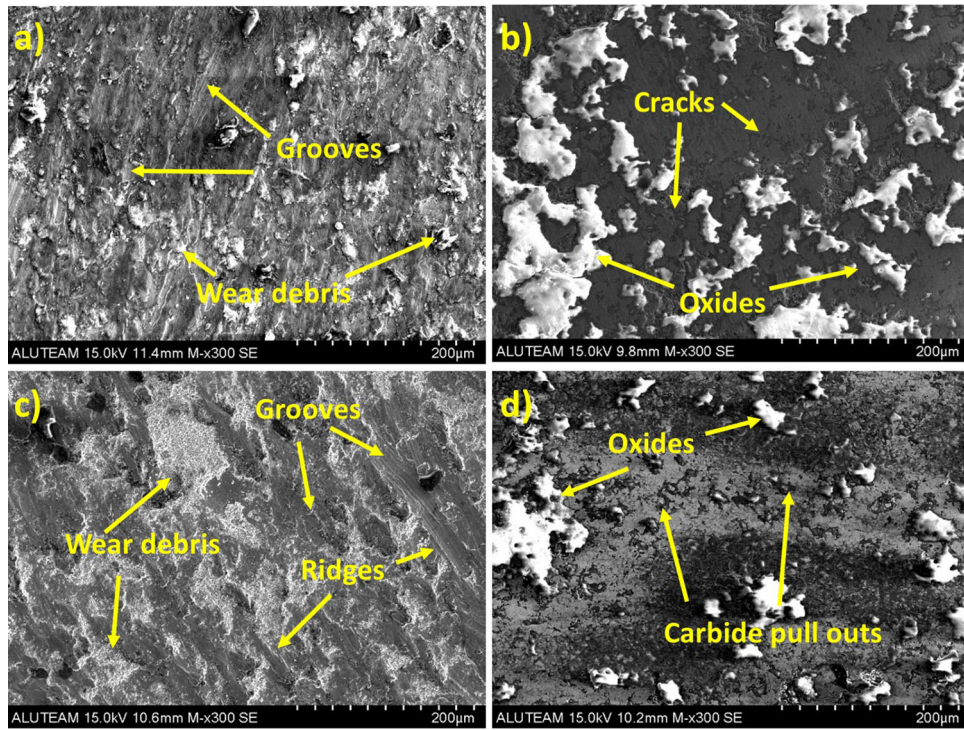
Fig. 12 Worn surface of the samples (a) AISI 2205 at 5N test load, (b) Cr_3C_2-NiCr/AISI 2205 at 5N test load, (c) AISI 2205 at 20N test load, (d) Cr_3C_2-NiCr/AISI 2205 at 20N test load

(Fig. 12b). Also, oxides were also detected on the wear surface. An unstable interaction of the Cr_3C_2-NiCr coating and Al_2O_3 counterface caused the formation of cracks due to an impact effect of the test load (Ref 64). Increasing test load enhanced the coating and counterface interaction, and carbide pull outs were observed. Formation of carbide pull outs with the increasing test load increased the wear damage, as seen in Fig. 12(d).

Figure 13 shows the 2D and 3D profile analyses of the samples. According to 2D profile analyses, wear depth of the AISI 2205 DSS at 5 N and 20 N test loads was determined as 35.35 μm and 62.61 μm, respectively. Moreover, wear depth of the Cr_3C_2-NiCr coated AISI 2205 DSS at 5 N and 20 N test loads was determined as 4.43 μm and 8.22 μm, respectively. It was seen that the wear scar depth was significantly reduced in the coated samples compared to AISI 2205 DSS. The coating consisting of hard Cr_3C_2 structures significantly reduced the wear depth of 2205 alloy. However, it was determined that increasing test load significantly affected the wear depth, and it shifted the wear depth of coated and uncoated samples to approximately twice the value. In 3D profile analyses, a deep wear scar formation was observed in uncoated samples at both test loads. In addition, increasing test load induced a significant increase in the width of the wear track. It was deduced that a shallow wear track is formed in the coated samples, compared to the uncoated sample.

The coefficient of friction (CoF) values of the worn samples can be seen in Fig. 14(a). The CoF values of the alloys were recorded between 0.35 and 0.65. The CoF values of the samples worn at 5 N showed heavy fluctuations. This

phenomenon can be attributed the stick-slip effect between the workpiece and counterface (Ref 65). The multi-phase structure of the substrate and coating caused the stick-slip effect at lower load. The severe interaction between the workpiece and counterface reduced the stick-slip effect with increasing test load, and the CoF reached steady-state condition after a certain sliding distance. In other respect, the CoF values of the coated samples were reduced compared to AISI 2205 DSS. The hard Cr_3C_2 particles in the coating improved wear behavior and the CoF values were decreased. Moreover, the coating included oxide structures that reduced the CoF by providing the lubricant effects (Ref 66).

The wear rate values were given in Fig. 14(b). The wear rate results were compatible with the results of the analyses given previously. In AISI 2205 DSS alloy, the wear rate doubled with the test load value increasing from 5 to 20 N. The wear rate was significantly increased in Cr_3C_2-NiCr coated AISI 2205 DSS alloy. The presence of carbides on the surface increased the wear resistance, and the oxides reduced the wear damage by acting as a lubricant. As a result, the dry sliding wear test results showed that the wear behavior of AISI 2205 DSS alloy was improved with Cr_3C_2-NiCr coating, and the wear losses were significantly reduced.

4. Conclusion

The corrosion and wear behaviors of the Cr_3C_2-NiCr coating on AISI 2205 DSS were investigated in this study. The coating was deposited on the AISI 2205 DSS alloy by
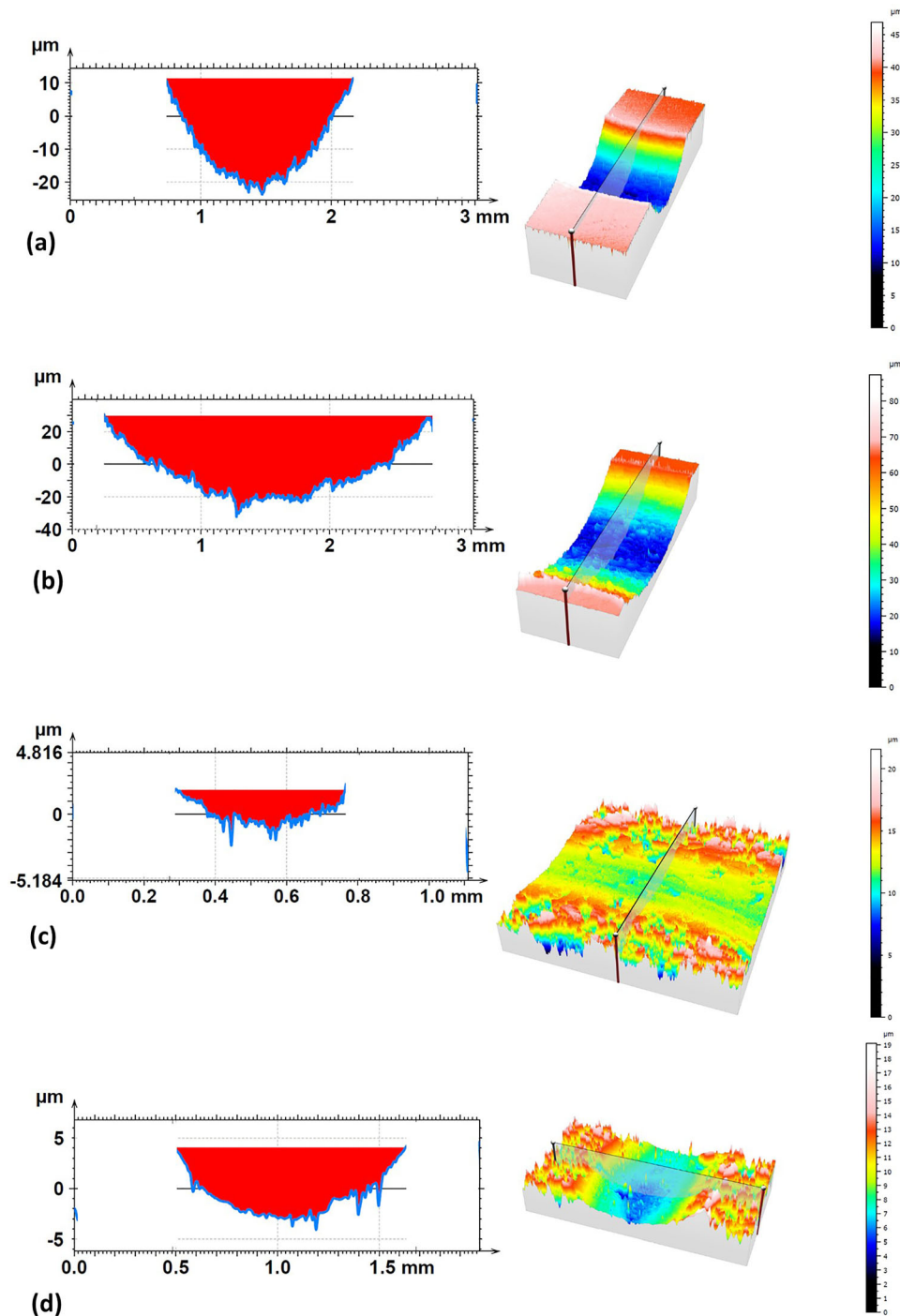
**Fig. 13** Worn surface of the samples (a) AISI 2205 at 5N test load, (b) AISI 2205 at 20N test load, (c) Cr_3C_2-NiCr/AISI 2205 at 5N test load, (d) Cr_3C_2-NiCr/AISI 2205 at 20N test load

HVOF technique. The results of the study can be summarized as follows:

The Cr_3C_2-NiCr coating was successfully coated on AISI 2205 DSS alloy using HVOF technique. As a result of microstructure investigations, it was observed that a proper bonding structure was obtained at the interface. In the upper layer of the coating, an angular particle morphology was obtained, and the angular structure transformed to spherical particle morphology toward the bottom layer of the coating.

As a result of electrochemical corrosion tests, a higher corrosion rate was obtained in the sample with Cr_3C_2-10%NiCr coating. Moreover, a higher weight loss value was obtained in the coated sample after immersion corrosion tests. However, the microstructure analyses showed that the pits were formed on the surface of the uncoated sample. The coating protected the substrate material by preserving the structure of the Cr_3C_2-10%NiCr on the sample surface.
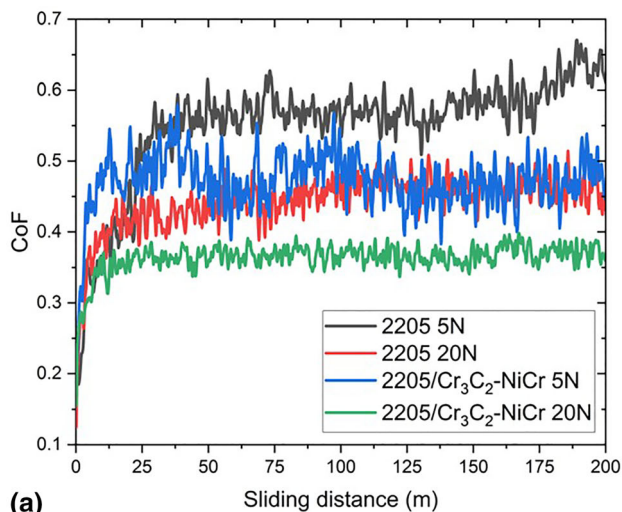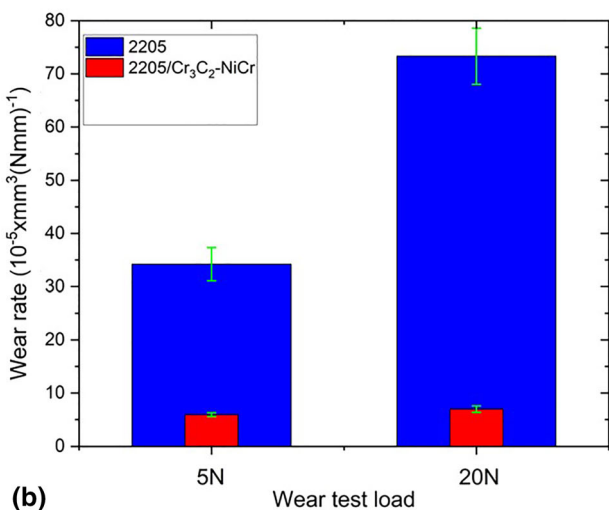
Fig. 14 Wear test results of the coated and uncoated AISI 2205. (a) CoF values, (b) Wear rate values

It was determined that Cr_3C_2-10%NiCr coating significantly increased the wear properties of AISI 2205 DSS alloy. In the wear test with 20 N test load, the wear rate of AISI 2205 DSS alloy was reduced from $73.32 \pm 5.28 \times 10^{-5}$ to $6.97 \pm 0.61 \times 10^{-5}$ mm^3 (Nmm)$^{-1}$ with Cr_3C_2-10%NiCr coating.

Acknowledgments

References

1. R. Badji, M. Bouabdallah, B. Bacroix, C. Kahloun, K. Bettahar, and N. Kherrouba, Effect of Solution Treatment Temperature on the Precipitation Kinetic of σ-Phase in 2205 Duplex Stainless Steel Welds, *Mater. Sci. Eng. A*, 2008, **496**(1-2), p 447–454. https://doi.org/10.1016/j.msea.2008.06.024

2. R. Francis and G. Byrne, Duplex Stainless Steels—Alloys for the 21st Century, *Metals*, 2021, **11**(5), p 836. https://doi.org/10.3390/met11050836

3. S.K. Ghosh and S. Mondal, High Temperature Ageing Behaviour of a Duplex Stainless Steel, *Mater Charact*, 2008, **59**(12), p 1776–1783. https://doi.org/10.1016/j.matchar.2008.04.008

4. A. Kisasoz, S. Gurel, and A. Karaaslan, Effect of Annealing Time and Cooling Rate on Precipitation Processes in a Duplex Corrosion-Resistant Steel, *Met. Sci. Heat Treat.*, 2016, **57**(9-10), p 544–547. https://doi.org/10.1007/s11041-016-9919-5

5. V.A. Hosseini, L. Karlsson, S. Wessman, and N. Fuertes, Effect of Sigma Phase Morphology on the Degradation of Properties in a Super Duplex Stainless Steel, *Materials*, 2018, **11**(6), p 933. https://doi.org/10.3390/ma11060933

6. E.A. Melo and R. Magnabosco, Influence of the Heterogeneous Nucleation Sites on the Kinetics of Intermetallic Phase Formation in Aged Duplex Stainless Steel, *Metall. Mater. Trans. A Phys. Metall. Mater. Sci.*, 2017, **48**(11), p 5273–5284. https://doi.org/10.1007/s11661-017-4299-z

7. E.M. Cojocaru et al., Influence of Ageing Treatment on Microstructural and Mechanical Properties of a Solution Treated UNS S32750/EN 1.4410/F53 Super Duplex Stainless Steel (SDSS) Alloy, *J. Market. Res.*, 2020, **9**(4), p 8592–8605. https://doi.org/10.1016/j.jmrt.2020.05.127

8. A. Kisasoz, A. Karaaslan, and Y. Bayrak, Effect of Etching Methods in Metallographic Studies of Duplex Stainless Steel 2205, *Met. Sci. Heat Treatm.*, 2017, **58**(11-12), p 704–706. https://doi.org/10.1007/s11041-017-0081-5

9. R.O. Sousa, P. Lacerda, P.J. Ferreira, and L.M.M. Ribeiro, On the Precipitation of Sigma and Chi Phases in a Cast Super Duplex Stainless Steel, *Metall. Mater. Trans. A Phys. Metall. Mater. Sci.*, 2019, **50**(10), p 4758–4778. https://doi.org/10.1007/s11661-019-05396-6

10. R. Wang, Precipitation of Sigma Phase in Duplex Stainless Steel and Recent Development on its Detection by Electrochemical Potentiokinetic Reactivation: A Review, *Corros. Commun.*, 2021, **2**, p 41–54. https://doi.org/10.1016/j.corcom.2021.08.001

11. Y. Xiao et al., Corrosion Behavior of 2205 Duplex Stainless Steel in NaCl Solutions Containing Sulfide İons, *Corros. Sci.*, 2022, **200**, p 110240. https://doi.org/10.1016/j.corsci.2022.110240

12. Y. Zhou and D.L. Engelberg, Fast Testing of Ambient Temperature Pitting Corrosion in Type 2205 Duplex Stainless Steel by Bipolar Electrochemistry Experiments, *Electrochem. Commun.*, 2020, **117**, p 106779. https://doi.org/10.1016/j.elecom.2020.106779

13. C. Örnek, K. Davut, M. Kocabaş, A. Bayatlı, and M. Ürgen, Understanding Corrosion Morphology of Duplex Stainless Steel Wire in Chloride Electrolyte, *Corros. Mater. Degrad.*, 2021, **2**, p 397–411. https://doi.org/10.3390/cmd2030021

14. D.D.S. Silva, T.A. Simões, D.A. Macedo, A.H.S. Bueno, S.M. Torres, and R.M. Gomes, Microstructural İnfluence of Sigma Phase on Pitting Corrosion Behavior of Duplex Stainless Steel/NaCl Electrolyte Couple, *Mater. Chem. Phys.*, 2021, **259**, p 124056. https://doi.org/10.1016/j.matchemphys.2020.124056

15. Y. Guo, J. Hu, J. Li, L. Jiang, T. Liu, and Y. Wu, Effect of Annealing Temperature on the Mechanical and Corrosion Behavior of a Newly Developed Novel Lean Duplex Stainless Steel, *Materials*, 2014, **6**(9), p 6604–6619. https://doi.org/10.3390/ma7096604

16. H. Hwang and Y. Park, Effects of Heat Treatment on the Phase Ratio and Corrosion Resistance of Duplex Stainless Steel, *Mater. Trans.*, 2009, **50**(6), p 1548–1552. https://doi.org/10.2320/matertrans.MER2008168

17. F. Marques, W.M. Da Silva, J.M. Pardal, S.S.M. Tavares, and C. Scandian, Influence of Heat Treatments on the Micro-abrasion Wear Resistance of a Superduplex Stainless Steel, *Wear*, 2011, **271**(9-10), p 1288–1294. https://doi.org/10.1016/j.wear.2010.12.087

18. M.B. Davanageri, S. Narendranath, and R. Kadoli, Influence of Heat Treatment on Microstructure, Hardness and Wear Behaviour of super Duplex Stainless Steel AISI 2507, *Am. J. Mater. Sci.*, 2015, **5**, p 48–52. https://doi.org/10.5923/c.materials.201502.10

19. J.L. del Abra-Arzola, M.A. Garcia-Renteria, V.I. Cruz-HErnandez, J. Garcia-Guerra, V.H. Martinez-Landeros, L.A. Falcon-Franco, and F.F. Curiel-Lopez, Study of the Effect of sigma Phase Precipitation on the Sliding Wear and Corrosion Behaviour of Duplex Stainless Steel AISI 2205, *Wear*, 2018, **400-401**, p 43–51. https://doi.org/10.1016/j.wear.2017.12.019

20. J.K. Sahu, U. Krupp, R.N. Ghosj, and H.J. Christ, Effect of 475 °C Embrittlement on the Mechanical Properties of Duplex Stainless Steel, *Mater. Sci. Eng. A*, 2009, **508**, p 1–14. https://doi.org/10.1016/j.msea.2009.01.039

21. M. Pohl and O. Storz, Sigma-Phase in Duplex-Stainless Steels, *Z. Met.*, 2004, **95**(7), p 631–638

22. H. Sieurin and R. Sandström, Sigma Phase Precipitation in Duplex Stainless Steel 2205, *Mater. Sci. Eng. A*, 2007, **444**, p 271–276. https://doi.org/10.1016/j.msea.2006.08.107

23. L.K. de Paula Inácio, W. Wolf, B.C.B. de Leucas, G.C. Stumpf, and D.B. Santos, Microtexture Evolution of Sigma Phase in an Aged Fine-Grained 2205 Duplex Stainless Steel, *Mater Charact*, 2021, **171**, p 110802. https://doi.org/10.1016/j.matchar.2020.110802

24. R. Subbiah, V. Vinod Kumar, and G. Lakshmi Prasanna, Wear Analysis of Treated Duplex Stainless Steel Material by Carburizing Process—A Review, *Mater. Today: Proc.*, 2019, **26**, p 2946–2952. https://doi.org/10.1016/j.matpr.2020.02.608

25. O. Palma Calabokis, Y. Núñez de la Rosa, C.M. Lepienski, R. Perito Cardoso, and P.C. Borges, Crevice and Pitting Corrosion of Low Temperature Plasma Nitrided UNS S32750 Super Duplex Stainless Steel, *Surf. Coat. Technol.*, 2021, **413**, p 127095. https://doi.org/10.1016/j.surfcoat.2021.127095

26. J.O.P. Neto et al., Wear and Corrosion Study of Plasma Nitriding F53 Super Duplex Stainless Steel, *Mater. Res.*, 2016, **19**(6), p 1241–1252. https://doi.org/10.1590/1980-5373-MR-2015-0656

27. R. Goyal, B.S. Sidhu, and V. Chawla, Hot Corrosion Performance of Plasma-Sprayed Multiwalled Carbon Nanotube-Al_2O_3 Composite Coatings in a coal-Fired Boiler at 900 °C, *J. Mater. Eng. Perform.*, 2020, **29**, p 5738–5749. https://doi.org/10.1007/s11665-020-05070-8

28. R. Goyal, B. Sidhu, and V. Chawla, Characterization of Plasma-Sprayed Carbon Nanotube (CNT)-Reinforced Alumina Coatings on ASME-SA213-T11 Boiler Tube Steel, *Int. J. Adv. Manuf. Technol.*, 2017, **92**(9-12), p 3225–3235. https://doi.org/10.1007/s00170-017-0405-z

29. G. Singh, N. Bala, V. Chawla, and Y.K. Singla, Hot Corrosion Behavior of HVOF-Sprayed Carbide based Composite Coatings for Boiler Steel in Na_2SO_4-60% V_2O_5 Environment at 900° C under Cyclic Conditions, *Corros. Sci.*, 2021, **190**, p 109666. https://doi.org/10.1016/j.corsci.2021.109666

30. S. Yin, J. Cizek, X. Suo, W. Li, and H. Liao, Thermal Spray Technology, *Adv. Mater. Sci. Eng.*, 2019, **2019**, p 8654764. https://doi.org/10.1155/2019/8654764

31. G.C.M. Patel, N.B. Pradeep, L. Girisha, H.M. Harsha, and A.K. Shettigar, Experimental Analysis and Optimization of Plasma Spray Parameters on Microhardness and Wear Loss of Mo-Ni-Cr Coated Super Duplex Stainless Steel, *Aust. J. Mech. Eng.*, 2022, **20**(5), p 1426–1438. https://doi.org/10.1080/14484846.2020.1808760

32. K. Singh, K. Goyal, and R. Goyal, Hot Corrosion Behaviour of Different Cr_3C_2-NiCr Coatings on Boiler Tube Steel at Elevated Temperature, *World J. Eng.*, 2019, **16**(4), p 452–459. https://doi.org/10.1108/WJE-02-2019-0049

33. A. Singh, K. Goyal, and R. Goyal, An Investigation on Hot Corrosion Behaviour of Cermet Coatings in Simulated Boiler Environment, *J. Bio- Tribo-Corros.*, 2019, **5**, p 86. https://doi.org/10.1007/s40735-019-0278-9

34. V.P.S. Sidhu, K. Goyal, and R. Goyal, Corrosion Behaviour of HVOF Sprayed Coatings on ASME SA213 T22 Boiler Steel in an Actual Boiler Environment, *Adv. Eng. Forum*, 2017, **20**, p 1–9. https://doi.org/10.4028/www.scientific.net/AEF.20.1

35. S. Hong et al., Microstructure and Cavitation-Silt Erosion Behavior of High-Velocity Oxygen-Fuel (HVOF) Sprayed Cr3C2-NiCr Coating, *Surf. Coat. Technol.*, 2013, **225**, p 85–91. https://doi.org/10.1016/j.surfcoat.2013.03.020

36. Z. Zhang, X. Lu, and J. Luo, Tribological Properties of Rare Earth Oxide Added Cr_3C_2-NiCr Coatings, *Appl. Surf. Sci.*, 2007, **253**(9), p 4377–4385. https://doi.org/10.1016/j.apsusc.2006.09.040

37. V.Y. Ulianitsky, I.S. Batraev, D.K. Rybin, D.V. Dudina, A.A. Shtertser, and A.V. Ukhina, Detonation Spraying of Cr_3C_2-NiCr Coatings and their Properties, *J. Therm. Spray Technol.*, 2022, **31**(3), p 598–608. https://doi.org/10.1007/s11666-021-01301-z

38. J.M. Guilemany, J. Fernandez, J. Delgado, A.V. Benedetti, and F. Climent, Effects of thickness coating on the electrochemical behaviour of thermal spray Cr_3C_2-NiCr coatings, *Surf. Coat. Technol.*, 2002, **153**, p 107–113

39. G.C. Ji, C.J. Li, Y.Y. Wang, and W.Y. Li, Microstructural Characterization and Abrasive Wear Performance of HVOF Sprayed Cr_3C_2-NiCr Coating, *Surf. Coat. Technol.*, 2006, **200**(24), p 6749–6757. https://doi.org/10.1016/j.surfcoat.2005.10.005

40. P.S. Kevin, A. Tiwari, S. Seman, S.A.B. Mohamed, and R. Jayaganthan, Erosion-Corrosion Protection due to Cr_3C_2-NiCr Cermet Coating on Stainless Steel, *Coatings*, 2020, **10**(11), p 1–17. https://doi.org/10.3390/coatings10111042

41. B.B. Mishra and H. Nautiyal, Frictional and Wear Behavior of Cr_3C_2-NiCr Coating on AISI-304 Stainless Steel, *Adv. Mater. Process. Technol.*, 2022, **8**(4), p 4007–4017. https://doi.org/10.1080/2374068X.2022.2036508

42. M. Majunatha, R.S. Kulkarni, and M. Krishna, Investigation of HVOF Thermal Sprayed Cr_3C_2-NiCr Cermet Carbide Coatings on Erosive Performance of AISI 316 Molybdenum Steel, *Procedia Mater. Sci.*, 2014, **5**, p 622–629. https://doi.org/10.1016/j.mspro.2014.07.308

43. A.S. Hajare and C.L. Gogte, Comparative Study of Wear Behaviour of Thermal Spray HVOF Coating on 304 SS, *Mater. Today Proc.*, 2018, **5**, p 6924–6933. https://doi.org/10.1016/j.matpr.2017.11.354

44. D.H. Bhosale, W.S. Rathod, M. Nogaraj, and M. Nagaraj, High-Temperature Erosion and Sliding Wear of Thermal Sprayed WC-Cr_3C_2-Ni Coatings, *Mater. High Temp.*, 2021, **38**, p 464–474. https://doi.org/10.1080/09603409.2021.1979734

45. N.V. Abhijith, D. Kumar, and D. Kalyansundaram, Development of Single-Stage TiNbMoMnFe High-Entropy Alloy Coating on 304L Stainless Steel using HVOF Thermal Spray, *J. Therm. Spray Technol.*, 2022, **31**, p 1032–1044. https://doi.org/10.1007/s11666-021-01294-9

46. N. Abu-warda, A.J. Lopez, M.D. Lopez, and M.V. Utrilla, Ni20Cr Coating on T24 Steel Pipes by HVOF Thermal Spray for High Temperature Protection, *Surf. Coat. Technol.*, 2020, **381**, p 125133. https://doi.org/10.1016/j.surfcoat.2019.125133

47. S. Singh and M. Kaur, Mechanical and Microstructural Properties of NiCrFeSiBC/Cr_3C_2 Composite Coatings—Part I, *Surf. Eng.*, 2016, **32**, p 464–474. https://doi.org/10.1179/1743294414Y.0000000416

48. J.O. Park, S. Matsch, and H. Böhni, Effects of Temperature and Chloride Concentration on Pit Initiation and Early Pit Growth of Stainless Steel, *J. Electrochem. Soc.*, 2002, **149**(2), p B34. https://doi.org/10.1149/1.1430415

49. J.M. Guilemany, J. Nutting, and N. Llorca-Isern, Characterisation of Cr_3C_2-NiCr Cermet Powder for High Velocity Oxyfuel Spraying, *Powder Metall.*, 1994, **37**, p 289–292. https://doi.org/10.1179/pom.1994.37.4.289

50. Q. Feng, C. Jiang, Z. Xu, L. Xie, and V. Ji, Effect of Shot Peening on the Residual Stress and Microstructure of Duplex Stainless Steel, *Surf. Coat. Technol.*, 2013, **226**, p 140–144. https://doi.org/10.1016/j.surfcoat.2013.03.047

51. J.M. Guilemany, N. Espallargas, P.H. Suegama, and A.V. Benedetti, Comparative Study of Cr_3C_2-NiCr Coatings Obtained by HVOF and Hard Chromium Coatings, *Corros. Sci.*, 2006, **48**(10), p 2998–3013. https://doi.org/10.1016/j.corsci.2005.10.016

52. S.S. Chatha, H.S. Sidhu, and B.S. Sidhu, High Temperature Hot Corrosion Behaviour of NiCr and Cr_3C_2-NiCr Coatings on T91 Boiler Steel in an Aggressive Environment at 750 °C, *Surf. Coat. Technol.*, 2012, **206**(19-20), p 3839–3850. https://doi.org/10.1016/j.surfcoat.2012.01.060

53. W. Zhou, K. Zhou, Y. Li, C. Deng, and K. Zeng, High Temperature Wear Performance of HVOF-Sprayed Cr_3C_2-WC-NiCoCrMo and Cr_3C_2-NiCr hardmetal coatings, *Appl. Surf. Sci.*, 2017, **416**, p 33–44. https://doi.org/10.1016/j.apsusc.2017.04.132

54. A. Babu, D. Dzhurinskiy, S. Dautov, and P. Shorkinov, Structure and Electrochemical Behavior of Atmospheric Plasma Sprayed Cr_3C_2-NiCr Cermet Composite Coatings, *Int. J. Refract Metal Hard Mater.*, 2023, **111**, p 106105. https://doi.org/10.1016/j.ijrmhm.2023.106105

55. J. Du, F. Li, Y. Li, L. Wang, H. Lu, X. Ran, and X. Zhang, Influences of Plasma Arc Remelting on Microstructure and Service Performance of Cr_3C_2-NiCr/NiCrAl Composite Coating, *Surf. Coat. Technol.*, 2019, **369**, p 16–30. https://doi.org/10.1016/j.surfcoat.2019.04.037

56. R.S. Dutta, R. Purandare, A. Lobo, S.K. Kulkarni, and G.K. Dey, Microstructural Aspects of the Corrosion of Alloy 800, *Corros. Sci.*, 2004, **46**(12), p 2937–2953. https://doi.org/10.1016/j.corsci.2004.04.005

57. A. Szewczyk-Nykiel and J. Kazior, Effect of Aging Temperature on Corrosion Behavior of Sintered 17-4 PH Stainless Steel in Dilute Sulfuric Acid Solution, *J. Mater. Eng. Perform.*, 2017, **26**(7), p 3450–3456. https://doi.org/10.1007/s11665-017-2778-4

58. J. Pi, Y. Pan, J. Wu, and X. He, Influence of Minor Addition of in on Corrosion Resistance of Cu-based Bulk Metallic Glasses in 3.5% NaCl

Solution, *Xiyou Jinshu Cailiao Yu Gongcheng/Rare Metal Mater. Eng.*, 2014, **43**(1), p 32–35. https://doi.org/10.1016/s1875-5372(14)60047-3

59. Č Donik, A. Kocijan, D. Mandrino, I. Paulin, M. Jenko, and B. Pihlar, Initial Oxidation of Duplex Stainless Steel, *Appl. Surf. Sci.*, 2009, **255**(15), p 7056–7061. https://doi.org/10.1016/j.apsusc.2009.03.041

60. G. Özer, Investigation of Inhibitory Effects of Chitosan on Pitting and Electrochemical Corrosion Behavior Caused by Sigma Phase in Duplex Stainless Steels (DSS), *Prot. Met. Phys. Chem. Surf.*, 2022, **58**(1), p 176–189. https://doi.org/10.1134/S2070205122010154

61. T. Suter, E.G. Webb, H. Böhni, and R.C. Alkire, Pit Initiation on Stainless Steels in 1 M NaCl With and Without Mechanical Stress, *J. Electrochem. Soc.*, 2001, **148**(5), p B174. https://doi.org/10.1149/1.1360204

62. Z. Wei, D. Cui, Z. Wei, and S. Hong, HVOF spray of Cr_3C_2-NiCr Coating for Enhancing the Corrosion Resistance of Nickel Aluminium Bronze in 3.5% NaCl Solution with Different Sulphide Concentrations, *J. Market. Res.*, 2023, **23**, p 869–881. https://doi.org/10.1016/j.jmrt.2023.01.050

63. M. Hoseinpoor, M. Momeni, M.H. Moayed, and A. Davoodi, EIS Assessment of Critical Pitting Temperature of 2205 Duplex Stainless Steel in Acidified Ferric Chloride Solution, *Corros. Sci.*, 2014, **80**, p 197–204. https://doi.org/10.1016/j.corsci.2013.11.023

64. K. Bobzin, L. Zhao, M. Öte, T. Königstein, and M. Steeger, Impact Wear of an HVOF-Sprayed Cr_3C_2-NiCr Coating, *Int. J. Refract. Metals Hard Mater.*, 2018, **70**, p 191–196. https://doi.org/10.1016/j.ijrmhm.2017.10.011

65. G. Özer et al., Effect of Heat Treatments on the Microstructure and Wear Behaviour of a Selective Laser Melted Maraging Steel, *Proc. Inst. Mech. Eng. Part E: J. Process Mech. Eng.*, 2022, **236**(6), p 2526–2535. https://doi.org/10.1177/09544089221093994

66. H.M. Khan, M.S. Yilmaz, S.S. Karabeyoğlu, A. Kisasoz, and G. Özer, Dry Sliding Wear Behavior of 316 L Stainless Steel Produced by Laser Powder Bed Fusion: A Comparative Study on Test Temperature, *Mater. Today Commun.*, 2023, **34**, p 105155. https://doi.org/10.1016/j.mtcomm.2022.105155